Measuring oxygen solubility in Ni grains and boundaries after oxidation using atom probe tomography ☆

Jonathan D. Poplawsky [a],*, Rishi Pillai [b],*, Qing-Qiang Ren [a], Andrew J. Breen [c], Baptiste Gault [d,e], Michael P. Brady [b]

[a] Center for Nanophase Materials Sciences, Oak Ridge National Laboratory, Oak Ridge, TN, USA
[b] Materials Science and Technology Division, Oak Ridge National Laboratory, Oak Ridge, TN, USA
[c] School of Aerospace, Mechanical & Mechatronic Engineering, and Australian Centre for Microscopy & Microanalysis, The University of Sydney, Sydney, NSW, Australia
[d] Max-Planck-Institut für Eisenforschung, Max-Planck-Str. 1, 40237 Düsseldorf, Germany
[e] Department of Materials, Royal School of Mines, Imperial College, Prince Consort Road, London SW7 2BP, UK

A R T I C L E   I N F O

A B S T R A C T

Poor oxidation resistance is a key contributor to material failure within extreme environments. Understanding oxygen solubility is important for computation aided design of new high strength, high-temperature oxidation resistant alloys. Oxygen solubility within pure metals, such as Ni, has been studied using a multitude of techniques, but Atom Probe Tomography (APT) has not been used for such a measurement to date. APT is the only technique offering both a high chemical sensitivity ($<$10 ppm) and resolution ($<$1 nm) allowing for a composition measurement within nms of the oxide/metal interface. APT was employed to measure the oxygen content at different depths from the oxide/metal interface as well as grain boundaries for a high and low purity Ni sample oxidized at 1000 °C for 48 h. The results reveal $<$10 s of ppm oxygen solubility within Ni metal at all depths and 100 s of ppm oxygen within GBs.

© 2021 The Authors. Published by Elsevier Ltd on behalf of Acta Materialia Inc.
This is an open access article under the CC BY license (http://creativecommons.org/licenses/by/4.0/)

The demand for efficiency enhancements and emission reductions in the power generation and transportation industries is driving operating temperatures higher than before [1,2]. Enabling multiple energy sources requires new high temperature materials that can withstand increasingly harsher environments [3]. Consequently, high temperature corrosion is amongst one of the life-limiting degradation mechanisms that must be addressed during alloy development.

Recent progress in computation hardware and software has enabled computation aided alloy design to be an efficient and effective method for designing new alloys [4–9]. However, modeling high-temperature corrosion is extremely challenging due to the lo-cal nature of the processes that can be influenced by a combination of factors. Although there has been significant progress in predicting oxidation induced degradation [6,10,11], there is no comprehensive model to predict multicomponent alloy high temperature oxidation behavior. Most high temperature alloys rely on surface chromia or alumina scales for oxidation protection [12]. Formation of the desired scale depends on the oxide thermodynamic stability, oxygen solubility, diffusivity of oxygen and element(s) forming the oxide scale, temperature, oxygen partial pressure, and oxide particle nucleation density [13,14]. Quantitative information on each of these parameters is essential to oxidation resistant alloy development. Yet, the experimental determination of dissolved oxygen has received limited attention because of challenges with detecting light elements in low concentration with high spatial resolution [15–18].

There are several studies that measured oxygen solubility in pure Ni metal, including those by Seybolt and Fullman [15], Alcock and Brown [19], and Park and Altstetter [16]. These three pivotal studies showed 100 s of ppm oxygen solubilities for temperatures ranging from 700–1200 °C, agreeing well with expected theoretical solubilities in Ni (Sievert's equation) [20]. The Ni was polycrystalline in these studies making the delineation of GB effects impossible.

Perusin et al. [21] used time-of-flight secondary ion mass spectrometry (TOF-SIMS) to study the oxygen solubility in Ni, which has a spatial resolution able to delineate grains from GBs. The results showed 50–100 times less (~1–10 ppm) intragranular dissolved oxygen than those reported previously, and that the oxygen did not diffuse greater than ~1 μm into the metallic grains. Furthermore, μm sized voids with high surface oxygen contents and NiO particles were found within grain boundaries (GBs) using SIMS and transmission electron microscopy (TEM), but oxygen within pristine GBs was unable to be detected due to spatial resolution constraints. Woodford and Bricknell showed GB embrittlement after oxidation in Ni and detected NiO particles on fractured surfaces, but this study also lacked a direct measurement of oxygen within pristine GBs [22,23]. A higher resolution technique such as atom probe tomography (APT) is better suited for directly identifying oxygen within GBs.

Here, we have employed APT to understand the oxygen solubility in high and low purity Ni. APT is a direct projection microscopy technique with sub-nm resolution and aa <10 ppm sensitivity [24–28]. Unfortunately, oxygen quantification is challenging because some field evaporated oxide molecules can be undetectable due to multi-hit detection events or molecular ion disassociation after field evaporation [29–32]. On the other hand, the detection of residual oxygen gas from the ultra-high vacuum (~10–11 Torr) analysis chamber can increase the measured oxygen concentration. Despite these challenges, dissolved oxygen within nms of the oxide scale interface and within GBs in oxidized high and low purity Ni was measured with APT. This information can be used to improve computational models and accelerate material development designed for extreme environments.
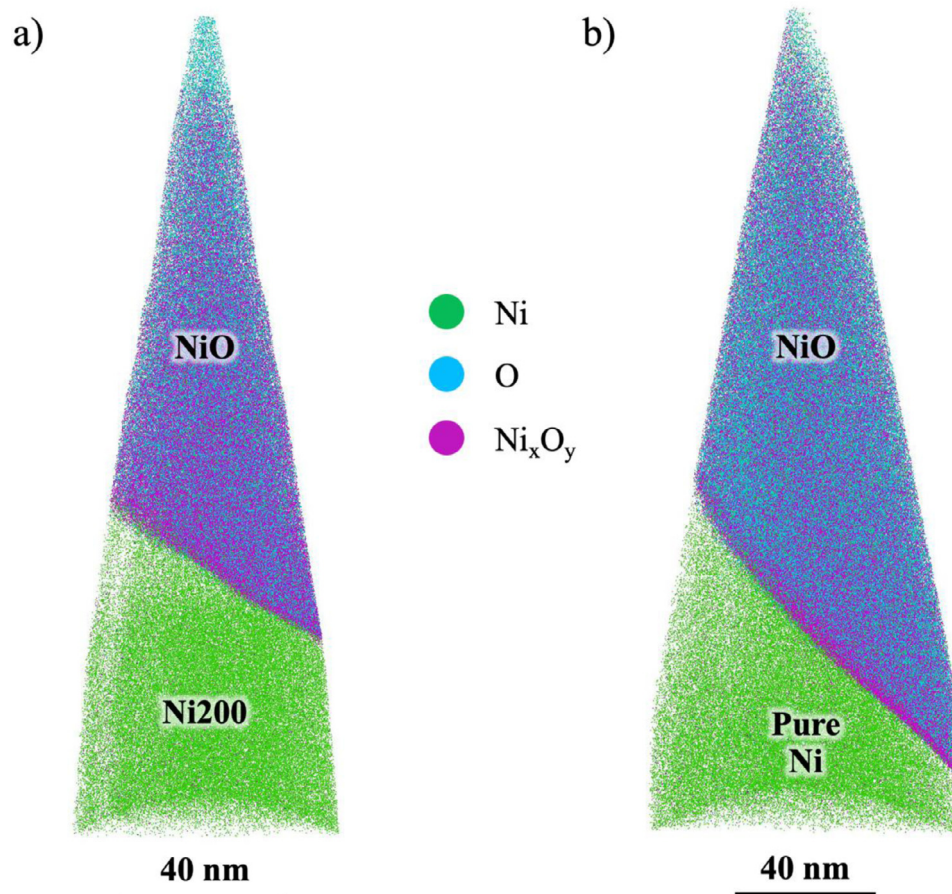
Table 1
Measured composition of the investigated alloys. Ni is in wt.% or at.% and the rest of the elements are in wppm or appm.

Alloy	Ni	O	Si	Mn	Cu	Fe	Na
Pure Ni (wt.)	99.999	14	0.04	0.003	0.015	-	0.03
Ni200 (wt.)	Bal.	5	200	2400	600	400	–
Pure Ni (at.)	99.89	51.3	0.084	0.003	0.014	–	0.009
Ni200 (at.)	Bal.	18.3	418	2564	554	420	–

The chemical compositions of the studied alloys are given in Table 1 using inductively coupled plasma atomic emission spectroscopy (ICP-AES), combustion-infrared absorbance (carbon), and inert gas fusion (oxygen). Alloy coupons ($10\times20\times1.5$ mm) were ground to a 600-grit finish and ultrasonically cleaned in acetone and methanol prior to oxidation. The pure Ni sample was placed in a quartz ampoule backfilled with $^{18}O_2$ gas at 1 atm. The Ni200 sample was exposed to dry laboratory air. Both samples were isothermally annealed for 48 h at 1000 °C. The pure Ni sample (^{18}O-Ni) was oxidized in an $^{18}O_2/^{16}O_2$ environment due to slight $^{16}O_2$ contamination. 1 atm $^{18}O_2$ gas was used to ensure that the partial pressure did not fall below 0.21 atm during the test. The oxidation kinetics (scale thickness) for each sample were similar.

APT specimens were fabricated with an FEI Nova 200 dual beam scanning electron microscope (SEM)/focused ion beam (FIB) instrument using the method described by Thompson et al. [33]. The APT experiments were run using a CAMECA LEAP 4000XHR in laser mode with a 30 K base temperature, a 60–70 pJ laser power, a 0.2% detection rate, and a 200 kHz pulse repetition rate. The APT results were crytallographically calibrated [34], and analyzed using

Fig. 1. APT atom maps of the oxide/metal interfaces of (a) ^{16}O-Ni200 (Ni200) and (b) ^{18}O-Ni (Pure Ni) samples oxidized at 1000 °C for 48 hrs. The Ni, O, and Ni_xO_y ions are displayed as green, light blue, and magenta dots, respectively.

Table 2

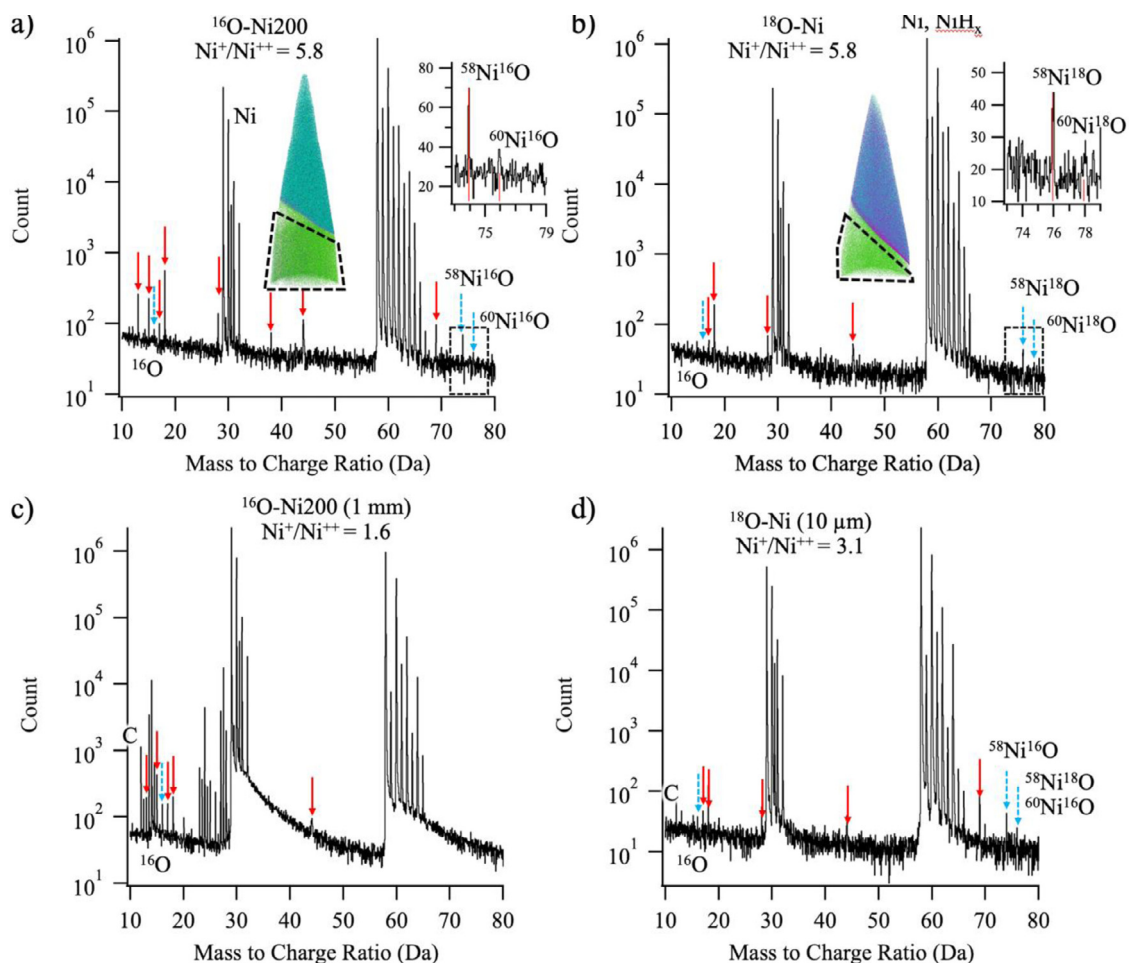The O composition for the ^{18}O-Ni and ^{16}O-Ni200 samples measured at different distances from the metal/oxide interface calculated from the mass spectra shown in Fig. 2. The compositions were calculated using only the ^{16}O$^+$, ^{58}Ni^{16}O$^+$, ^{60}Ni^{16}O$^+$, ^{58}Ni^{18}O$^+$, and ^{60}Ni^{18}O$^+$ mass spectral peaks only when present in the mass spectrum. All vacuum gas peaks, such as HO, H$_2$O, CO$_2$ etc., were ignored. All reported values are background corrected using IVAS's local range assisted background subtraction method. The "noise" was calculated by ranging regions before and after the mass spectral peaks used for oxygen quantification. This value is also background corrected. The error is the standard error and does not account for non-quantifiable error [36].

Location	Sample	APT measured oxygen (ppm)
~20–200 nm from int.	^{18}O-Ni	44±3
	^{16}O-Ni200	49±3
~10 µm from int.	^{18}O-Ni	16±1
>1 mm from int.	^{16}O-Ni200	26±2
Noise	N/A	~10

CAMECA's IVAS 3.8 software. The misorientation of the APT dataset grain boundaries were measured using the protocol outlined by Breen et al. [35]. The error presented in the proximity histograms and Table 2 is the standard error [25]. This value does not represent the total error because phenomena such as residual oxygen in the vacuum chamber and preferential loss of oxygen can add to error but is difficult to quantify.

APT atom maps for the metal/oxide interface for ^{18}O-Ni and ^{16}O-Ni200 are shown in Fig. 1. Much care needs to be taken when determining the low metal oxygen content because there are mass spectral peak overlaps that need to be considered. ^{18}O$_2$ and ^{16}O$_2$ oxidation experiments were conducted to differentiate residual APT chamber vacuum gas from oxygen within the specimen and to determine the molecular state oxygen is detected. Mass spectra from volumes in the APT data are displayed in Fig. 2.

Some mass spectral peak overlaps of concern are the ^{16}O$_2$$^+$, ^{64}Ni^{2+} peak overlap at 32 Da and the ^{18}O, ^{1}H$_2$^{16}O peak overlap at 18 Da ^{1}H^{16}O (17Da) because ^{1}H$_2$^{16}O (18 Da) mass spectral peaks are commonly found in APT data due to residual water vapor (^{1}H$_2$^{16}O) in the vacuum chamber ionizing at the specimen surface. In addition, the specimen's oxygen can bind with vacuum H before field evaporation. It is impossible to delineate residual vacuum water vapor from the sample's oxygen binding with residual vacuum H when the sample contains ^{16}O; however, the absence of mass spectral peaks at 19 and 20 Da relating to H^{18}O$^+$ and H$_2$^{18}O$^+$ for the ^{18}O-Ni samples (Fig. 2b and d) proves that it is unlikely for residual H to bind to oxygen on the Ni surface before field evaporation and subsequent detection, and therefore, the peaks at 17 and 18 Da can be ignored. Unfortunately, a reliable ^{18}O$^+$ measurement is impossible at 18 Da due to residual water vapor detection.

Fig. 2. Mass spectra for (a)^{16}O-Ni200 close to the oxide/metal interface, (b) ^{18}O-Ni close to the interface, (c) ^{16}O-Ni200 1 mm from the interface, and (d) ^{18}O-Ni 10 µm from the interface. The insets of (a) and (b) are zoomed in regions of the NiO$^+$ peaks with the expected isotopic abundancies marked by the red lines. Large volumes containing millions of ions were used to increase the sensitivity of the measurement. The dashed black polygons show the volume used for producing the mass spectra in (a) and (b). All oxide related peaks used for calculating the composition are marked with blue dotted arrows. From left to right: ^{16}O (16 Da). ^{58}Ni^{16}O (74 Da), ^{60}Ni^{16}O and ^{58}Ni^{18}O (76 Da), and ^{60}Ni^{18}O (78 Da). The red arrows indicate vacuum gasses and FIB Ga ions, which were not used for the compositional analysis. From left to right in (a), the red arrows identify CN^{2+}, NO^{2+}, HO$^+$, H$_2$O$^+$, N$_2$$^+$, NiH$_2$^{16}O^{2+}, CO$_2$$^+$, and Ga$^+$. The Ni$^+$/Ni^{++} charge-state-ratios are displayed for each mass spectrum.

The ^{18}O oxidized samples (Fig. 2b and d) do not show mass spectral peaks for $^{16}O^{18}O^+$ or $^{18}O_2{}^+$ at 34 Da and 36 Da, respectively, proving that molecular O_2 in the metal solid-solution is not a field evaporation product. The ^{16}O-Ni200 specimen shows $^{58}Ni^{16}O^+$ and $^{60}Ni^{16}O^+$ peaks at 74 and 76 Da (Fig. 2a) while the ^{18}O-Ni specimen shows $^{58}Ni^{18}O^+$ and $^{60}Ni^{18}O^+$ peaks at 76 and 78 Da (Fig. 2b). The mass spectra do not show ^{61}NiO, ^{62}NiO, and ^{64}NiO peaks due to the low abundance of these Ni isotopes. The NiO peaks are the dominant oxide peaks as they have 2 and 4 times more counts than the ^{16}O peak for ^{16}O-Ni200 and ^{18}O-Ni, respectively. The ^{16}O-Ni200 mass spectrum also shows a peak at 38 Da (Fig. 2a), which can only be $^{58}Ni^1H_2{}^{16}O$ as this sample was exposed to $^{16}O_2$. Therefore, the 38 Da peak is interpreted as a vacuum gas and is ignored for the O concentration measurement. These results indicate that O is predominately detected as NiO$^+$ when within the metal solid solution at low concentrations.

APT specimens were also made from an intermediated depth and the center of the sample ($\sim$10 μm and 1 mm from the oxide scale, respectively) for the ^{18}O-Ni and ^{16}O-Ni200 samples. The $^{58}Ni^{16}O^+$ and $^{58}Ni^{18}O^+$ or $^{60}Ni^{16}O^+$ mass spectral peaks are present in the specimen made 10 μm from the interface (Fig. 2d), while the sample made $\sim$1mm from the interface does not show the existence of NiO$^+$ peaks (Fig. 2c). The measured O content calculated from all samples and depths are displayed in Table 2.

The Ni^{18}O peaks at 76 and 78 Da shown in Fig. 2b proves that O within solid solution is detectable by APT, which has been specified with an approximately 10 ppm sensitivity. An underestimation of the O content due to the preferential loss of O was previously discussed, but we must also consider an overestimation of O in this case because the measured O content is close to APT's detection limit. O^+ at 16 Da can be a result of O in the analysis chamber despite the UHV conditions. Additionally, FIB specimen preparation and sample transfer could induce oxidation [37], although we carefully selected regions that were least affected by FIB damage in the APT data to mitigate this concern. To this end, the oxygen content from these APT measurements is interpreted as having the same value (10 s of ppm) to compensate for non-quantifiable error.

This result is consistent with the SIMS work published by Perusin et al. [21] ($\sim$1–10 ppm), adding confidence. SIMS has a higher chemical sensitivity than APT meaning that the SIMS measured intragranular oxygen content is probably more reliable, however, APT has a much higher spatial resolution. Large volumes within the APT data were used to calculate the oxygen content displayed in Table 2 to increase the measurement sensitivity, which decreases the resolution.

A closer investigation of the metal/oxide interface was achieved using proximity histograms with 2 nm bins ($\sim$200,000 ions/bin) from planar 15 at.% O isoconcentration surfaces (the oxide metal interface) for ^{16}O-Ni200 and ^{18}O-Ni (displayed in Fig. 3). Sigmoidal functions, $f(x) = \frac{O_{max}}{1+e^{-\frac{x \pm x_0}{\tau}}}$, were fit to the proximity histograms with 4τ defined as the interfacial width [38]. The measured interfacial widths from the sigmoidal fits are 3.5 and 4.3 nm for the ^{16}O-Ni200 and ^{18}O-Ni samples, respectively. These measured interfacial widths were relatively the same using <1 nm bins. The APT measured interfacial widths are most likely wider than the actual interface width due to APT aberrations [39–43].

The voltage curve for the ^{16}O-Ni200 APT experiment displayed in Fig. 3(b) maintains a parabolic shape indicating that there is no noticeable difference in the evaporation field of the NiO and Ni metal, and therefore, trajectory aberrations at the interface should be minimal [41]. In Fig. 3(c)-(f), the O profiles match the sigmoidal fits almost perfectly for both samples, and at closer inspection (Fig. 3(d),(f)), it is clear that the O content reaches its baseline value immediately after the interface, which is tabulated in Table 2.
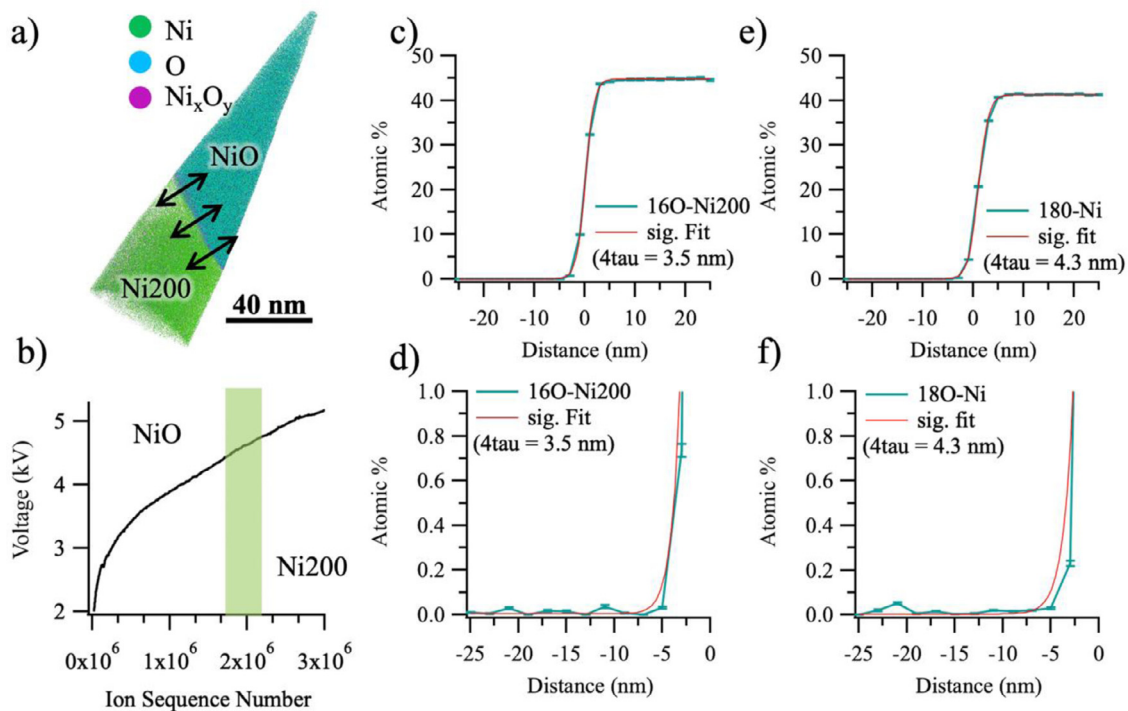
Fig. 3. (a) An APT atom map of the ^{16}O-Ni200 sample with arrows showing the proximity histogram location. (b) The voltage curve for the ^{16}O-Ni200 sample with the green rectangle highlighting the presence of the interface on the needle surface during the experiment. (c) A proximity histogram across the Ni200/NiO interface from the ^{16}O-Ni200 sample. (d) The proximity histogram in (c) with adjusted y-axis values. (e) A proximity histogram across the NiO/Ni interface for the ^{18}O-Ni sample. (f) The proximity histogram in (e) with adjusted y-axis values. The proximity histograms were calculated from a 15 at.% O isoconcentration surface using 2 nm bins and a local range assisted background subtraction. Sigmoidal fits to the data are also displayed with the interfacial widths denoted by 4tau.
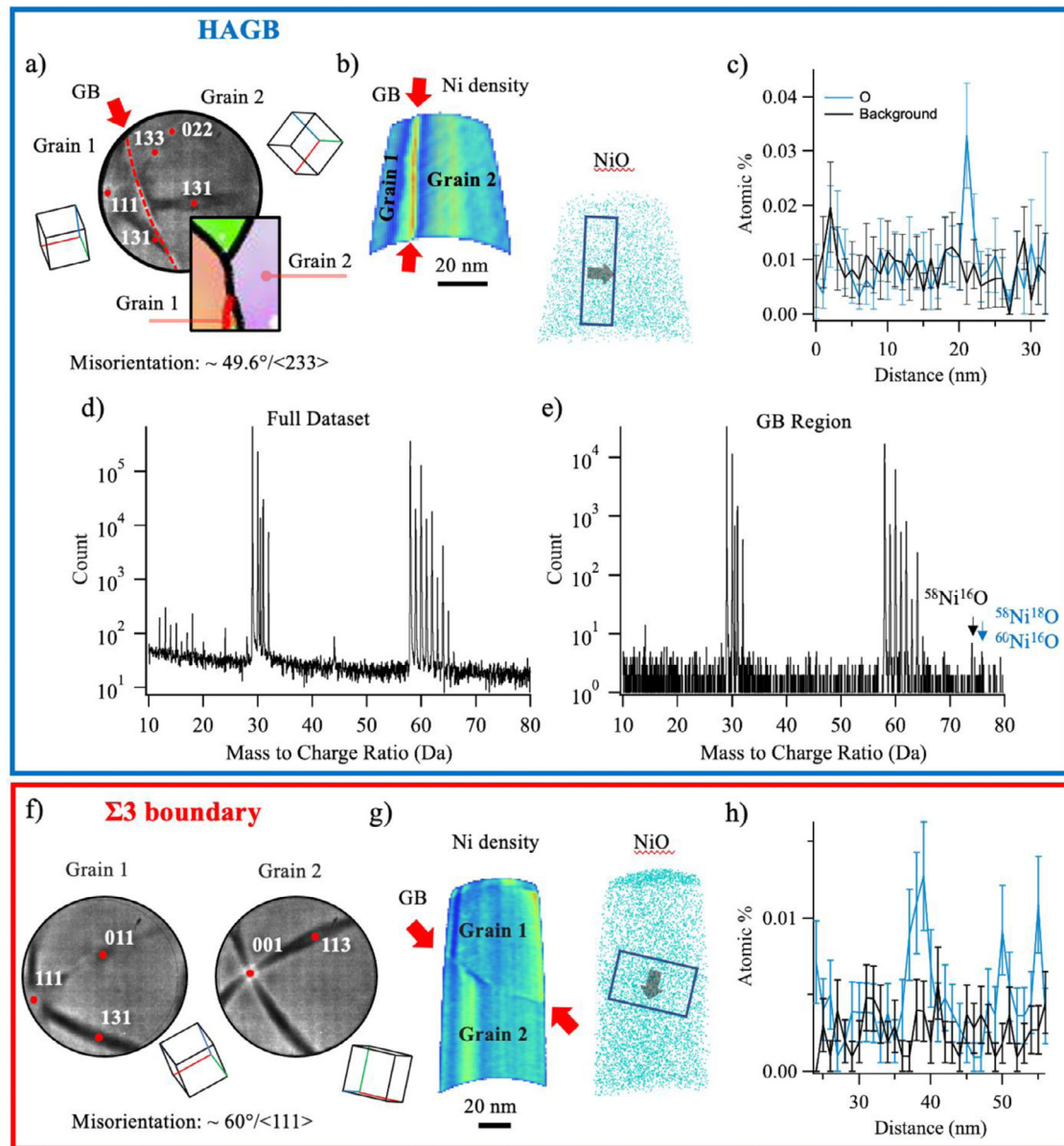
Fig. 4. Ni GB oxygen measurement. HAGB: (a) The APT detector event histogram showing a clear GB in the field of view with the poles highlighted. The inset is an EBSD inverse pole figure (IPF-Z) with the grains in the APT field of view marked. The black lines are HAGBs, and the red line is a $\Sigma3$ GB. b) APT density map of Ni to highlight the GB region in the reconstruction and a NiO atom map with the 1DCP region of interest indicated. (c) A 1DCP of the HAGB displayed in (a) and (b) showing the oxygen and oxygen background concentrations. Mass spectra of the (d) full dataset and (e) extracted GB region. $^{58}Ni^{16}O$ and $^{58}Ni^{18}O$ or $^{60}Ni^{16}O$ peaks are only visible in the extracted GB region. $\Sigma3$ GB: (f) the APT detector event histograms for 2 grains captured in the dataset with the poles indexed. (g) Ni density map showing the GB region and a NiO atom map with the 1DCP region of interest indicated. (h) The corresponding $\Sigma3$ GB 1DCP indicating an increased oxygen content within the GB.

Overall, a low oxygen content (10 s of ppm) has been detected within Ni metal from within nms and up to 1 mm from the oxide interface using APT.

Electron backscatter diffraction (EBSD) and site-selective FIB sample preparation was used to prepare a high angle GB (HAGB) approximately 20 μm from the oxide/metal interface in the ^{18}O-Ni sample, displayed in Fig. 4(a). A clear GB between two grains with different orientations is found within the APT detector event histogram containing this HAGB. The Ni density map displayed in Fig. 4(b) shows an increased density in the GB location, which is common in APT data due to GB trajectory aberrations [41]. The NiO species ($^{58}Ni^{16}O$ and $^{58}Ni^{18}O$ or $^{60}Ni^{16}O$) atom map, although noisy, also shows an increased density within the GB. A 1D concentration profile across the HAGB shows an increased O content within the GB with a maximum value of 260 ppm after back-

ground subtraction (Fig. 4(c)). It is likely that the maximum O concentration is indeed higher than 260 ppm because broadening of the GB in the APT data underestimates the GB concentration [44]. Background is also included in the 1D concentration profile (1DCP), which was ranged before and after the oxide peaks in the mass spectrum.

Mass spectra for the full dataset and the GB region are displayed in Fig. 4(d) and (e). The full dataset mass spectrum shows several vacuum gas and Ni peaks, but no visible NiO^+ peaks. The only non-Ni peaks within the GB mass spectrum are at 14, 74, and 76 Da, which are N^+ (potentially vacuum gas), $^{58}Ni^{18}O$ or $^{60}Ni^{16}O$, respectively. The counts within the 76 Da peak are ~3 times larger than the expected counts for $^{60}Ni^{16}O$ given the counts in the 74 Da peak ($^{58}Ni^{16}O^+$), suggesting that there is a $^{58}Ni^{18}O^+$ peak overlapped with the $^{60}Ni^{16}O$ peak; however, there

is not a noticeable ^{60}Ni^{18}O peak at 78 Da. Therefore, it is possible that ^{18}O from the oxidation experiment infiltrated this HAGB. The ^{58}Ni^{16}O$^+$ peak could be oxygen from the oxidation experiment due to contamination or inherent oxygen in the as-fabricated Ni specimen.

APT was also conducted on a symmetric $\Sigma 3$ GB with the results displayed in Fig. 4(f). Direct measurement of the misorientation of this boundary from the APT data confirmed a $60°/<111>$ angle/axis pair, characteristic of this special low energy boundary. The grain boundary normal for each grain was also directly measured from the APT data and found to be close to $\langle 221 \rangle$ in each case. The common grain boundary normal in each grain and the relative flatness of the boundary suggests that it is most likely a symmetric twin $\Sigma 3$. Excess oxygen was also detected at this boundary with a similar maximum concentration relative to the HAGB (100 ppm after background correction).

The measured intragranular oxygen content within high and low purity Ni using APT was found to be on the order of 10 s of ppm. Proximity histograms of the oxide/metal interface do not show oxygen diffusion greater than $\sim$1 nm into the metallic grains. These results are consistent with the SIMS analysis performed by Perusin et al. [21] and do not reproduce the historic bulk oxygen solubility studies and oxidation models ($>$100 ppm oxygen measured in solution). The key difference between these works is the spatial resolution of the techniques used to measure the oxygen concentration, i.e. being able to delineate GBs from grain interiors. The discrepancy is consistent with the hypothesis that oxygen diffuses and accumulates within GBs.

Excess oxygen was directly measured within pristine GBs by APT. The oxygen concentration (100 s of ppm) is too low to account for the bulk metal O concentration after oxidation measured by inert gas fusion (115 - 367 ppm). The "missing" oxygen is most likely bound within internal NiO precipitates, which were previously found in Ni GBs [21–23].

These results highlight that oxygen diffusion primarily occurs within GBs and there is minimal oxygen diffusion into the Ni grains even within nanoscale distances from the oxide scale. This finding provides guidance to the scientific community aiming to quantify dissolved oxygen in high temperature alloys at oxide/alloy interfaces. Rethinking oxidation models to include lower oxygen solubilities in grain interiors and to include GB diffusion mechanisms will be critical to the continuing efforts in the development of next generation oxidation resistant alloys for future energy landscapes.

Declaration of Competing Interest

The authors declare that they have no known competing financial interests or personal relationships that could have appeared to influence the work reported in this paper.

Acknowledgments

Supplementary materials

Supplementary material associated with this article can be found, in the online version, at doi:10.1016/j.scriptamat.2021.114411.

References

[1] D. Shifler, Mater. High Temp. 32 (1–2) (2015) 148–159.
[2] M. Schütze, W.J. Quadakkers, Oxid. Metals 87 (5) (2017) 681–704.
[3] J. Anderson, D. Rode, H.B. Zhai, P. Fischbeck, Energ. Policy 148 (2021).
[4] Y. Yamamoto, G. Muralidharan, M.P. Brady, Scr. Mater. 69 (11–12) (2013) 816–819.
[5] R. Pillai, K. Kane, M. Lance, B.A. Pint, Computational methods to accelerate development of corrosion resistant coatings for industrial gas turbines, Superalloys (2020) 2020.
[6] A. Chyrkin, R. Pillai, H. Ackermann, H. Hattendorf, S. Richter, W. Nowak, D. Gruner, W.J. Quadakkers, Corros. Sci. 96 (2015) 32–41.
[7] G.B. Olson, C.J. Kuehmann, Scr. Mater. 70 (2014) 25–30.
[8] G.B. Olson, Scr. Mater. 70 (2014) 1–2.
[9] G.B. Olson, Science 288 (5468) (2000) 993.
[10] R. Duan, A. Jalowicka, K. Unocic, B.A. Pint, P. Huczkowski, A. Chyrkin, D. Grüner, R. Pillai, W.J. Quadakkers, Oxid. Metals 87 (1) (2017) 11–38.
[11] B.A. Pint, R. Pillai, M.J. Lance, J.R. Keiser, Oxid. Metals 94 (5–6) (2020) 505–526.
[12] D.J. Young, High Temperature Oxidation and Corrosion of Metals, Elsevier, Oxford, 2008.
[13] C. Wagner, Zeitschrift fur Elektrochemie 63 (7) (1959) 772–790.
[14] C. Wagner, J. Electrochem. Soc. 99 (10) (1952) 369–380.
[15] A.U. Seybolt, R.L. Fullman, JOM 6 (5) (1954) 548–549.
[16] J.W. Park, C.J. Altstetter, Metallurgical Transactions A 18 (1) (1987) 43–50.
[17] J.H. Swisher, Turkdoga. Et, Trans. Metal. Soc. Aime 239 (4) (1967) 426 -&.
[18] D. Jullian, J.Q. Zhang, D.B. Hibbert, D.J. Young, J. Alloys Compd. 732 (2018) 646–654.
[19] C.B. Alcock, P.B. Brown, Metal Sci. J. 3 (1) (1969) 116–120.
[20] A. Sieverts, Zeitschrift für Metallkunde 21 (1929) 37–46.
[21] S. Perusin, D. Monceau, E. Andrieu, J. Electrochem. Soc. 152 (12) (2005) E390.
[22] D.A. Woodford, R.H. Bricknell, Metall. Mater. Trans. A 12 (8) (1981) 1467–1475.
[23] R.H. Bricknell, D.A. Woodford, Metal. Trans. A 12 (3) (1981) 425–433.
[24] D.J. Larson, T. Prosa, R.M. Ulfig, B.P. Geiser, T.F. Kelly, New York, US: Springer Science (2013).
[25] M.K. Miller, Atom Probe Tomography, Springer US, Boston, MA, 2000.
[26] F. De Geuser, B. Gault, Acta Mater. 188 (2020) 406–415.
[27] B.M. Jenkins, F. Danoix, M. Gouné, P.A.J. Bagot, Z. Peng, M.P. Moody, B. Gault, Microsc. Microanal. 26 (2) (2020) 247–257.
[28] D. Haley, A.J. London, M.P. Moody, Microsc. Microanal. 26 (5) (2020) 964–977.
[29] B. Gault, D.W. Saxey, M.W. Ashton, S.B. Sinnott, A.N. Chiaramonti, M.P. Moody, D.K. Schreiber, New J. Phys. 18 (3) (2016) 033031 -17.
[30] A. Devaraj, R. Colby, W.P. Hess, D.E. Perea, S. Thevuthasan, J. Phys. Chem. Lett. 4 (6) (2013) 993–998.
[31] R. Kirchhofer, D.R. Diercks, B.P. Gorman, J.F. Ihlefeld, P.G. Kotula, C.T. Shelton, G.L. Brennecka, J. Am. Ceramic Soc. 97 (9) (2014) 2677–2697.
[32] R. Kirchhofer, M.C. Teague, B.P. Gorman, J. Nucl. Mater. 436 (1) (2013) 23–28.
[33] K. Thompson, D. Lawrence, D.J. Larson, J.D. Olson, T.F. Kelly, B. Gorman, Ultramicroscopy 107 (2–3) (2007) 131–139.
[34] B. Gault, M.P. Moody, F. de Geuser, G. Tsafnat, A. La Fontaine, L.T. Stephenson, D. Haley, S.P. Ringer, J. Appl. Phys. 105 (3) (2009) 034913.
[35] A.J. Breen, K. Babinsky, A.C. Day, K. Eder, C.J. Oakman, P.W. Trimby, S. Primig, J.M. Cairney, S.P. Ringer, Microsc. Microanal. 23 (2) (2017) 279–290.
[36] M.K. Miller, R.G. Forbes, Atom-probe Tomography: the Local Electrode Atom Probe, 2014.
[37] L.T. Stephenson, A. Szczepaniak, I. Mouton, K.A.K. Rusitzka, A.J. Breen, U. Tezins, A. Sturm, D. Vogel, Y. Chang, P. Kontis, A. Rosenthal, J.D. Shepard, U. Maier, T.F. Kelly, D. Raabe, B. Gault, PLoS ONE 13 (12) (2018) e0209211.
[38] O. Dyck, D.N. Leonard, L.F. Edge, C.A. Jackson, E.J. Pritchett, P.W. Deelman, J.D. Poplawsky, Adv. Mater. Interfaces 4 (21) (2017).
[39] D.J. Larson, B. Gault, B.P. Geiser, F. De Geuser, F. Vurpillot, Curr. Opin. Solid State Mater. Sci. 17 (5) (2013) 236–247.
[40] F. Vurpillot, B. Gault, B.P. Geiser, D.J. Larson, Ultramicroscopy 132 (C) (2013) 19–30.
[41] F. Vurpillot, A. Bostel, D. Blavette, Appl. Phys. Lett. 76 (21) (2000) 3127 -4.
[42] D.J. Larson, T.J. Prosa, B.P. Geiser, W.F. Egelhoff, Ultramicroscopy 111 (6) (2011) 506–511.
[43] J.G. Brons, A.A. Herzing, K.T. Henry, I.M. Anderson, G.B. Thompson, Thin Solid Films 551 (C) (2014) 61–67.
[44] J.D. Poplawsky, C. Li, N.R. Paudel, W. Guo, Y. Yan, S.J. Pennycook, Sol. Energy Mater. Sol. Cells 150 (C) (2016) 95–101.